International Journal of Computational Methods
Vol. 14, No. 2 (2017) 1750047 (18 pages)

DOI: 10.1142/S0219876217500475

Combined Discrete–Finite Element Modeling of Ballasted Railway Track Under Cyclic Loading

S. Shao[*,‡], Y. Yan[†,§] and S. Ji[*,¶]

[*]*State Key Laboratory of Structural Analysis for Industrial Equipment Dalian University of Technology, Dalian 116024, P. R. China*

[†]*School of Civil and Safety Engineering Dalian Jiaotong University, Dalian 116028, P. R. China*

[‡]*shaoshuai@mail.dlut.edu.cn*
[§]*yyan@djtu.edu.cn*
[¶]*jisy@dlut.edu.cn*

Received 2 November 2015
Revised 16 August 2016
Accepted 27 September 2016
Published

This paper proposes a combined discrete–finite element model to investigate the dynamic behavior of ballasted railway tracks. The discrete element method (DEM) is adopted to model the discrete ballast materials. The shapes of ballast particles resembled clumps of overlapping spheres which are obtained by the growth of spheres inside convex polyhedrons. The finite element method (FEM) is used to analyze the continuous embankment and foundation. The transmission between DEM and FEM at the ballast-embankment interface is processed according to the interaction force based on the principle of virtual work. The dynamic behavior of ballasted railway track under cyclic loading is simulated with the developed DEM–FEM model. The settlement of the sleeper and the deformation of the embankment and foundation, the force chains in the ballast and stress distributions in the embankment and foundation are obtained. The developed model is helpful in better understanding the mechanical characteristics of ballasted railway tracks.

Keywords: Discrete element method; finite element method; combined algorithm; ballasted railway track; cyclic loading.

1. Introduction

Ballasted railway tracks usually consist of rails, fastening system, sleepers, ballast, subballast, embankment and foundation [Selig and Waters (1994)]. Under the repeated traffic loading, track geometry deteriorates due to track settlement induced by the rearrangement and breakage of ballast particles, deformation of the embankment and foundation. In particular, as a consequence of ever-increasing train speeds and axle loads, track settlement has become an important factor influencing directly

[¶]Corresponding author.

the safety, stability and ride comfort of the train. Thereby, a better fundamental understanding of the dynamic behavior of ballasted track as a whole and the interactions between track components plays a major role in reducing the maintenance costs of ballasted tracks and improving passenger comfort as well.

As a mature numerical simulation method, finite element method (FEM) has been adopted in the numerical analysis of the whole ballasted track structure [Li *et al.* (2015); Nejad (2014); Shahraki *et al.* (2015)]. Ballast, subballast, embankment and foundation are all treated as continuum with different material parameters measured from experiments. The vertical deflections have been studied by different combinations of parameters, such as the ballast thickness, the rail pad stiffness, the height and Young's modulus of the embankment and the sleeper spacing [Real *et al.* (2012)]. The effect of geocell confinement on ballast was studied via FEM analysis when a soft subgrade, weaker ballast, or varying reinforcement stiffness are encountered [Leshchinsky and Ling (2013)]. Moreover, a 3D finite element coupled train–track model was proposed to study the ground induced vibration caused by the passage of high-speed train. With this model, the relation between track deflection and train speed was investigated [Ei Kacimi *et al.* (2013)].

FEM-based studies provide a macroscopic insight of the dynamic behavior of ballasted tracks. However, the ballast layer is naturally made up of a large number of discrete ballast particles. Ballast particles present complex dynamic behavior during the particles' contact and breakage under traffic loading. The micro-properties of ballast, such as particles' sizes, gradation, void ratio, are the key parameters that influence the track's macro settlement. In particular, the ballast particles' shapes at micro-scale play an important role in determining its macro-mechanical behavior [Lu and McDowell (2007)]. Recently, a growing number of continuum constitutive models emerged with ingredients that stem directly form micro-mechanical features [Coleri *et al.* (2012)]. FEM using a continuum model can analyze micro-mechanical features in noncontinuum body quite well [Hai (2013); Ghauch *et al.* (2015)].

As an effective numerical tool for discontinuum, discrete element method (DEM) proposed by Cundall has been widely applied in simulating mechanical behavior of railway ballast alone [Cundall and Strack (1979); Lim and McDowell (2005); Lobo-Guerrero and Vallejo (2006); Lu and McDowell (2010); Ngo *et al.* (2014); Huang and Tutumluer (2011)]. Originally, simple shapes are used to model the ballast particles' shapes, such as spheres or disks [Lobo-Guerrero and Vallejo (2006); Chen *et al.* (2012); Indraratna *et al.* (2012)]. Several approaches to generate complex-shaped ballast stones are presented. Clumps formed by clumping and agglomerates formed by bonding multiple spheres are the two effective ways to model realistic particles because of the simple contact detection and force calculation between spheres. Clumped particles are created by clumping spheres with prescribed initial overlap without generating interaction force, and all of clumped particles move as one element that will not break apart [Peters and Džiugys (2002); Ferellec and McDowell (2010)]. Aggregates of bonded spheres, created by bonding regular particles without initial overlap, are allowed to break up under large inter-particle interaction and deformation [Potyondy and Cundall (2004); Yan *et al.* (2014)]. Recently, an image-aided DEM approach has also been proposed to study the performances and degradations of railway ballast [Huang and Tutumluer (2011); Zhao *et al.* (2006)]. Clumped particles and bonded particles are two valid elements to simulate ballast particles [Wang *et al.* (2015); Laryea *et al.* (2014)]. Clumped particles can simulate shape more accurately with lesser particles. While due to the large overlap, clumped particles are not well suited to modeling particle breakage. Contrary to clumped particles, bonded particles could simulate the breakage of particles quite well, but more particles are required to simulate accurate particle shape. In this paper, clumped particles are employed to analyze the dynamic behavior of ballast under traffic loading.

The interaction between ballast and its substructure is an interaction of granular media with continuous structure. The coupling of DEM with FEM is an effective approach for such problems. The DEM is used to model discrete particles and the FEM is used to model continuum structure. More attention has been paid to the coupled DEM–FEM in order to combine the advantages of noncontinuum and continuum-based modeling [Guo *et al.* (2016); Indraratna *et al.* (2015); Onate and Rojek (2004)]. By additional kinematic constraints imposed by means of either the Lagrange multipliers or penalty function method, the coupling between the DEM and FEM subdomains is provided [Rojek and Onate (2007)]. A coupling DEM–FEM is presented with rotations coupling, the proposed method provides a way to reduce spurious wave reflections [Rousseau *et al.* (2009)].

Considering various geometric characteristics of ballasted railway track components, different numerical methods need to be used to simulate the mechanical behavior of ballasted railway track. This paper aims to establish a three-dimensional combined discrete–finite element model to analyze the dynamic behavior of ballasted railway track under cyclic loading. The DEM is employed to model ballast stones, and FEM is used to model the embankment and foundation. A contact algorithm between FEM and DEM is proposed based on the principle of virtual work. With the developed model, the settlement of the sleeper, force chains of ballast, deformation and the stress distribution of the embankment and foundation are studied.

2. DEM–FEM Model of Ballasted Railway Track

Figure 1 shows the computational domain and the cross-section of a simplified ballasted railway track. The sleeper provides cyclic loading to ballast, and performs as a rigid body. Due to the different material natures of track components, the discrete ballast layer is modeled with DEM. The embankment and foundation layer are continuous and can be simulated with FEM. The mechanical parameters transmission between DEM and FEM is realized through a contact algorithm based on the principle of virtual work. The details of the DEM–FEM model of ballasted railway track are as follows.

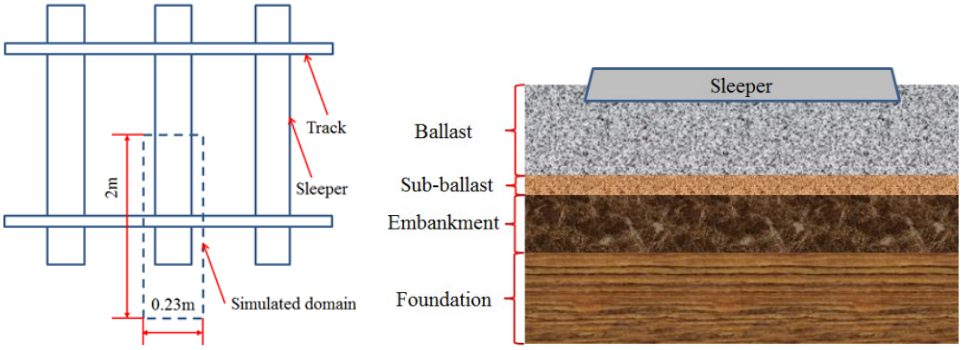

Fig. 1. The computational domain and the cross-section of the ballasted railway track.

2.1. *Discrete element model of ballast*

2.1.1. *Generation of ballast particle shapes*

Figure 2(a) shows a typical ballast stone featuring many planar surfaces. Here, a simple but practical approach is presented to reproduce its realistic shape [Ferellec and McDowell (2010)]. Firstly, an arbitrary convex polyhedron is generated and its surfaces are extracted as the ballast particle surfaces (Fig. 2(b)). Both of the size and shape of ballast are considered during the polyhedron generation. Secondly, a cubic domain encompassing the space enclosed by these surfaces is defined with a uniformly-sized assembly of spheres filled into it. Those spheres located inside the space enclosed by the ballast particle surfaces are remained to form the initial ballast particle (Fig. 3(a)). In order to make the spheres fitted to the surface contour of the generated ballast surfaces, a growth process of spheres is then started. The system is stabilized by a cycling process under gravity until the sphere radius reaches its maximum and the location of each sphere does not change distinctly (Fig. 3(b)). It should be noted that the number of spheres depends on the degree of precision in the simulation of clump shape. The accuracy of shape simulation in clump model increases with the increase of sphere number. In this paper, the initial diameter of

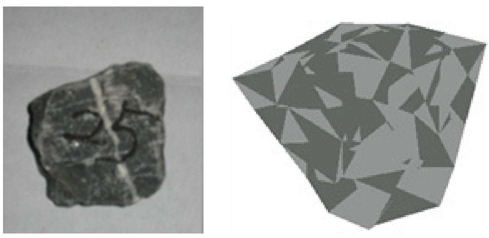

(a) (b)

Fig. 2. A typical ballast stone and corresponding convex polyhedron surfaces resembling its shape.

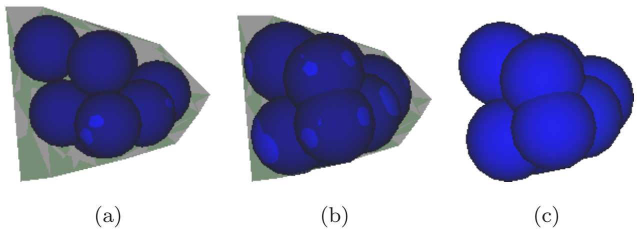

Fig. 3. The growth process of spheres inside the generated ballast surfaces.

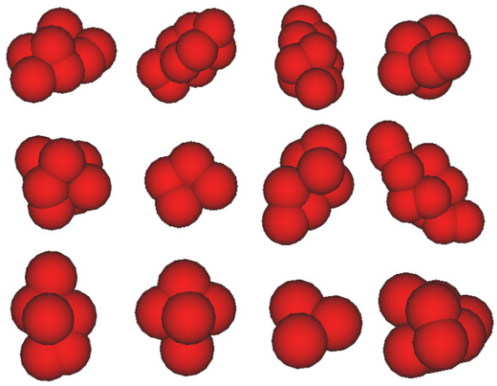

Fig. 4. Generated different ballast particles.

spheres is calculated by $D = (1/4)\sqrt[3]{(a \cdot b \cdot c)/N}$, D is the diameter, a, b and c are the maximal lengths of ballast stone in the three coordinate axis. N is the number of spheres. The generated final ballast particle is shown in Fig. 3(c).

Figure 4 shows ballast particles with different shapes constructed using this method. Each ballast particle consists of different number of spheres overlapped in different directions and behaves as a rigid body. The mass, center-of-mass and moment of inertia of a clump in the local coordinates are determined by using finite segment method [Yan and Ji (2010)]. Figure 5 shows the DEM model of the ballast layer, consisting of 1,727 clumps and 10,098 spheres.

2.1.2. *Contact force model*

The process of search for contacts between the clumps is potentially the most time consuming part of the simulation. The contact is registered when an overlap between two particles of two different clumps is detected. The process of search for contacts between the clumps is quite similar to that between particles [Cundall (1988)]. The difference between them is that the two detected particles mostly belongs to two different clumps. The simplest method of global search is to check for an overlap

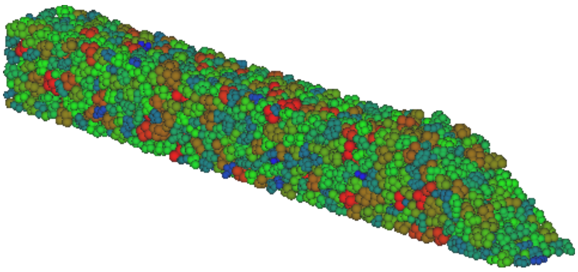

Fig. 5. DEM model of the ballast layer with clumped spheres.

between all pairs of particles. However, for large number of particles, this search procedure becomes prohibitively time consuming. Based on the idea of "neighborhood search", a more efficient search procedure is devised in this paper. The method for improving efficiency of search procedure is to keep short list of neighbors for each clump, and to search for contacts only among these neighbors.

In order to define a neighborhood about a particle of a clump, a rectangular grid is superimposed on to a space occupied by particles, as shown in Fig. 6. In this case, the area that needs to be searched for contacts of a given particle (target object) consists of $3^2 - 1$ cells surrounding the cell occupied by the particle. When the center of any particle in a clump locates in these neighbor cells, the particle is defined as a neighbor particle (Candidate Object) for the given particle. As shown in Fig. 6, the target object consists of four particles, the search procedure of Nos. 1 and 2 particles are given in this figure. When all the four particles are detected, the neighbor list of this clump is determined.

The contacts between clumps are contacts of two regular spheres. When the contact forces of all the particles in one clump is valued, the resultant force and moment acting on the center-of-mass of this clump can be determined according to

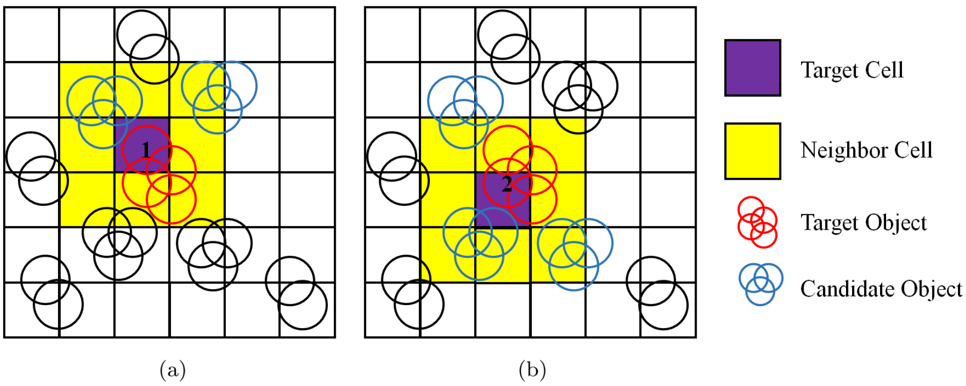

Fig. 6. The process of search for contacts between the clumps. (a) The possible contacts of No. 1 particle. (b) The possible contacts of No. 2 particle.

these contact forces. With the resultant force and moment, the movement of the clump can be calculated by Newton's second law. Based on Hertz's theory of the particle–particle contact of two elastic spheres, the normal contact force consists of elastic and viscous forces and can be written as [Ramirez *et al.* (1999)]

$$F_n = K_n x_n^{3/2} + \frac{3}{2} A K_n x_n^{1/2} \dot{x}_n. \tag{1}$$

Without considering the viscous force, and with the consideration of the Mohr–Coulomb friction law, the tangential contact force can be determined as [Di Renzo and Di Maio (2005)],

$$F_s^* = K_s x_n^{1/2} x_s, \tag{2}$$

$$F_s = \mathrm{sign}(F_s^*) \min(|F_s^*|, |\mu F_n|), \tag{3}$$

$$\mathrm{sign}(x) = \begin{cases} -1 & \text{if } x < 0, \\ 0 & \text{if } x = 0, \\ 1 & \text{if } x > 0, \end{cases} \tag{4}$$

where x_n and $\dot{x}_n$ are the normal deformation and deformation rate, respectively. x_s is the shear deformation and μ is the friction coefficient. F_s^* is current tangential force, the modulus of F_s^* should not be bigger than maximum static friction force. A is a material constant depending on the Young's modulus, viscous coefficients and Poisson ratio of the material and can be determined by the restitution coefficient of particle collisions at a certain speed [Ramirez *et al.* (1999)]. K_n and K_s in the above contact model can be calculated as [Di Renzo and Di Maio (2005)],

$$K_n = \frac{4}{3} E^* \sqrt{R^*}, \tag{5}$$

$$K_s = 8 G^* \sqrt{R^*}, \tag{6}$$

where $E^* = \frac{E}{2(1-\upsilon^2)}$, $G^* = \frac{G}{2(2-\upsilon)}$, $G = \frac{E}{2(1+\upsilon)}$, $R^* = \frac{R_A R_B}{R_A + R_B}$. E, υ and G are the Young's modulus, Poisson ratio and shear modulus of the ballast material. R_A and R_B are the radius of two particles in contact.

The maximum time step in the nonlinear DEM can be determined by [Kremmer and Favier (2001)],

$$t_{\max} = \frac{\pi R_{\min}}{0.163\upsilon + 0.8766} \sqrt{\frac{\rho}{G}}. \tag{7}$$

The real time-step in the calculation is less than the maximum, and is determined by,

$$\Delta t = \alpha t_{\max}, \tag{8}$$

where α is an empirical coefficient. Normally, with higher coordination number ($N_c > 4$), $\Delta t = 0.2 t_{\max}$, and with lower coordination number ($N_c < 4$), $\Delta t = 0.4 t_{\max}$ [Kremmer and Favier (2001)]. In this study, we set $\alpha = 0.2$.

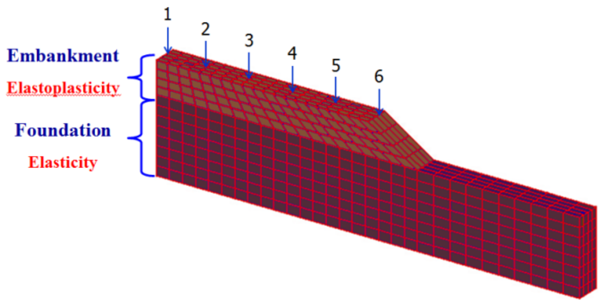

Fig. 7. FEM model of embankment and foundation.

2.2. *Finite element model of embankment and foundation*

Figure 7 shows the FEM model of the embankment and foundation. The model totally consists of 1,280 elements and 6,677 nodes. Each element has 20 isoparametric nodes. The boundary conditions imposed are as follows. The top surface of the embankment is free. The surface on both sides of the model in x-direction has restrictions on displacements along the x-axis. The surface on both sides of the model in y-direction has restrictions on displacements along the y-axis. The surface at the bottom of the model has restricted vertical displacements. Drucker–Prager yield criterion is employed to analyze the elastic–plastic response of the embankment, and elastic linear model is utilized to simulate the foundation.

The Newmark method is employed to analyze the dynamic response of embankment and foundation. The scheme of Newmark is as follows:

$$m\ddot{x}_{k+1} + c\dot{x}_{k+1} + kx_{k+1} = F_{k+1}, \tag{9}$$

$$\dot{x}_{k+1} = \dot{x}_k + (1-\delta)\Delta t\ddot{x}_k + \delta\Delta t\ddot{x}_{k+1}, \tag{10}$$

$$x_{k+1} = x_k + \dot{x}_k\Delta t + \left(\frac{1}{2} - \alpha\right)(\Delta t)^2\ddot{x}_k + \alpha(\Delta t)^2\ddot{x}_{k+1}, \tag{11}$$

where F_{k+1} is the external load of time t_{k+1}; δ and α are the parameters of Newmark method. The computational process is unconditional stability on condition that $\delta \geq 0.5$ and $\alpha \geq 0.25(0.5+\delta)^2$. Generally, $\delta = 0.5$ and $\alpha = 0.25$. Due to the nonlinear nature of embankment, Newton–Raphson method is utilized to solve the nonlinear dynamic equation in each time step of FEM [Winkel (2010)].

2.3. *Combined DEM–FEM model on ballast-embankment interface*

AQ: Please check we have changed Figure 7 to Figure 8. Is it ok?

Figure 8 is right.

Figure 8 depicts the contact between ballast clump and the top surface of the embankment. The transmissions of mechanical variables of the DEM and the FEM on the ballast-embankment interface are key factors to the established combined DEM–FEM model. The contact forces obtained from the DEM are the external loads acting on the FEM, and the deformation calculated from the FEM are the boundary conditions updated in the DEM. The contact forces from the DEM are not

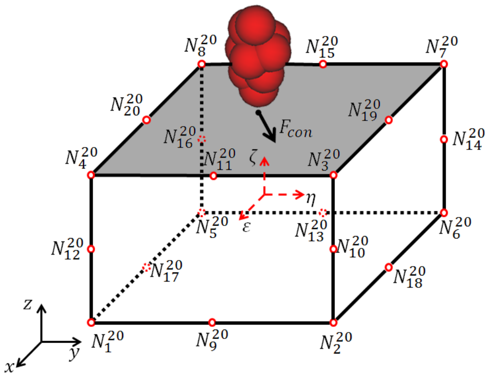

Fig. 8. Contact model of DEM and FEM on ballast-embankment interface.

always located right on the nodes of the finite element, which is the requirement of the FEM calculations. Here, the equivalent nodal loads acting on the finite element from the DEM contact forces are obtained based on the principle of virtual work.

The virtual work δW done by the DEM contact forces is given by,

$$\delta W = \delta U^T F_{\mathrm{con}}, \tag{12}$$

where F_{con} is contact force vector on the contact points between ballast clump and the top surface of the embankment. U is the displacement of contact point, which can be interpolated in terms of the nodal displacement u_i and the shape function of the FEM. Thus, the displacement field can be expressed as

$$U = N_i^{20} u_i, \quad i = 1\text{–}20, \tag{13}$$

where N_i^{20} is the shape function of 20-node isoparametric element evaluated at the contact point. u_i is the displacement of one element in x_k. Substituting Eq. (13) in to Eq. (12), we have,

$$\delta W = \delta u_i^T [N_i^{20}]^T F_{\mathrm{con}}, \quad i = 1\text{–}20. \tag{14}$$

The virtual work δW done by the FEM node forces is given by

$$\delta W = \delta u_i^T F_{\mathrm{nodal},i}, \quad i = 1\text{–}20. \tag{15}$$

Hence, the equivalent nodal forces $F_{\mathrm{nodal},i}$ in the local coordinate system can be expressed as,

$$F_{\mathrm{nodal},i} = [N_i^{20}]^T F_{\mathrm{con}}, \quad i = 1\text{–}20. \tag{16}$$

Here,

$$N_i^{20} = (1+\varepsilon_0)(1+\eta_0)(1+\varsigma_0)(\varepsilon_0+\eta_0+\varsigma_0-2)/8, \quad i = 1\text{–}8, \tag{17a}$$

$$N_i^{20} = (1-\varepsilon^2)(1+\eta_0)(1+\varsigma_0)/4, \quad i = 17\text{–}20, \tag{17b}$$

$$N_i^{20} = (1-\eta^2)(1+\varsigma_0)(1+\varepsilon_0)/4, \quad i = 9, 11, 13, 15, \tag{17c}$$

$$N_i^{20} = (1-\varsigma^2)(1+\varepsilon_0)(1+\eta_0)/4, \quad i = 10, 12, 14, 16, \tag{17d}$$

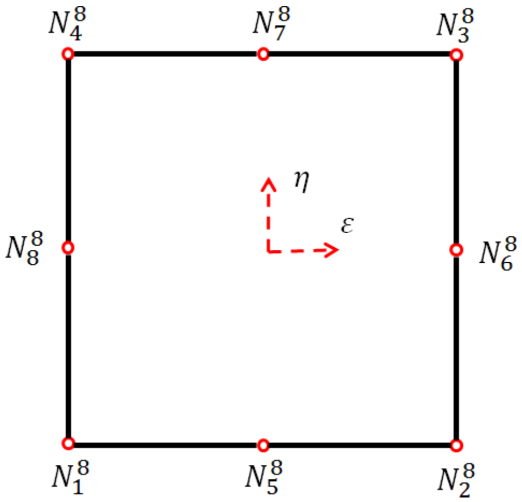

Fig. 9. The sketch of the eight-node isoparametric element for evaluation of ε and η.

$$\varepsilon_0 = \varepsilon_i \varepsilon, \quad \eta_0 = \eta_i \eta, \quad \varsigma_0 = \varsigma_i \varsigma, \tag{18}$$

where $(\varepsilon, \eta, \zeta)$, $(-1 \leq \varepsilon, \eta, \zeta \leq 1)$ are the coordinates of the contact points in the local coordinate system. Since the contact points are always located on the top surface of the embankment layer, ζ equals 1. The values of ε and η can be obtained with Newton iteration method by using the shape function for eight-node isoparametric element as shown in Fig. 9.

$$U_x = \sum_{i=1}^{8} N_i^8 u_{ix}, \quad U_y = \sum_{i=1}^{8} N_i^8 u_{iy}, \tag{19}$$

$$N_i^8 = -\frac{1}{4}(1 + \varepsilon_i \varepsilon)(1 + \eta_i \eta)(1 - \varepsilon_i \varepsilon - \eta_i \eta), \quad i = 1, 2, 3, 4, \tag{20a}$$

$$N_i^8 = \frac{1}{2}(1 - \varepsilon^2)(1 + \eta_i \eta), \quad i = 5, 7, \tag{20b}$$

$$N_i^8 = \frac{1}{2}(1 - \eta^2)(1 + \varepsilon_i \varepsilon), \quad i = 6, 8, \tag{20c}$$

where (x, y) is the coordinate of the contact point in the global coordinate system. (x_i, y_i) is the coordinate of element nodes in the global coordinate system. N_i^8 is the shape function of eight-node isoparametric element.

Let $f(\varepsilon, \eta) = x - \sum_{i=1}^{8} N_i^8 x_i = 0$ and $g(\varepsilon, \eta) = y - \sum_{i=1}^{8} N_i^8 y_i = 0$, the values of ε and η can be solved with Newton iteration method as follow:

$$\varepsilon = \varepsilon_k + \frac{f(\varepsilon_k, \eta_k) g_\eta(\varepsilon_k, \eta_k) - g(\varepsilon_k, \eta_k) f_\eta(\varepsilon_k, \eta_k)}{g_\varepsilon(\varepsilon_k, \eta_k) f_\eta(\varepsilon_k, \eta_k) - f_\varepsilon(\varepsilon_k, \eta_k) g_\eta(\varepsilon_k, \eta_k)}, \tag{21}$$

$$\eta = \eta_k + \frac{g(\varepsilon_k, \eta_k) f_\varepsilon(\varepsilon_k, \eta_k) - f(\varepsilon_k, \eta_k) g_\varepsilon(\varepsilon_k, \eta_k)}{g_\varepsilon(\varepsilon_k, \eta_k) f_\eta(\varepsilon_k, \eta_k) - f_\varepsilon(\varepsilon_k, \eta_k) g_\eta(\varepsilon_k, \eta_k)}, \tag{22}$$

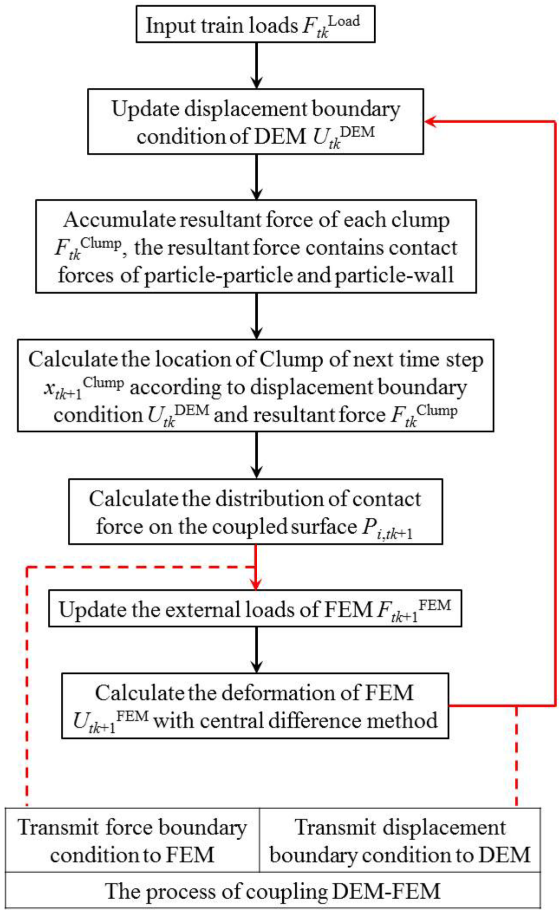

Fig. 10. The flow chart of combined DEM–FEM.

where ε_k and η_k are the initial approximations of ε and η, and $f_\varepsilon(\varepsilon_k, \eta_k) = \frac{\partial}{\partial \varepsilon} f(\varepsilon_k, \eta_k)$, $f_\eta(\varepsilon_k, \eta_k) = \frac{\partial}{\partial \eta} f(\varepsilon_k, \eta_k)$, $g_\varepsilon(\varepsilon_k, \eta_k) = \frac{\partial}{\partial \varepsilon} g(\varepsilon_k, \eta_k)$, $g_\eta(\varepsilon_k, \eta_k) = \frac{\partial}{\partial \eta} g(\varepsilon_k, \eta_k)$.

The combined discrete–finite element model (DEM, FEM) and the contact algorithm is coded by Fortran language. The flow chart of the combined discrete–finite element model is shown in Fig. 10.

3. Dynamic Behavior of Ballasted Track Under Cyclic Loading

Figure 11 shows the developed DEM–FEM model of ballasted railway track. The coordinate system is set on the lower left corner of foundation. The lengths of the top and bottom surface, and the height of the ballast layer are 1.5, 2.0, 0.3 m, respectively. The lengths of the top and bottom surface of the embankment are 2.0 and 2.5 m, respectively, and the height is 0.3 m. The length and height of the foundation are 4.0 and 0.7 m, respectively. In the model, x-axis, y-axis and z-axis

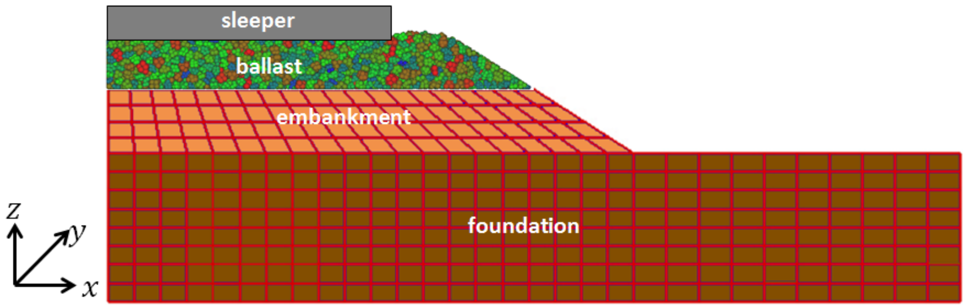

Fig. 11. The ballasted railway track model and axis directions.

represent the longitudinal, transverse and vertical direction, respectively. Usually, the required time increment of DEM is much smaller than that of FEM. In order to enhance the computational efficiency, the time increment of FEM is 40 times larger than that of DEM. The computational parameters used in the model are listed in Tables 1 and 2.

With the development of railway technology, train speed increases obviously. The maximum speed of high-speed railway has exceeded 250 km/h since 2009 in China. The axle load of CRH series is 14–17 ton. In this paper, 250 km/h and 15 ton are taken as an example. A cyclic loading with the amplitude of 75 kN is applied on the ballast layer at a frequency of 0.36 Hz. Figure 12 gives its time history and enlarged view of one load cycle. The enlarged view of one load cycle is shown in Fig. 12(b). This cyclic loading was obtained by using vehicle–track coupled model proposed by Zhai *et al.* [2010]. In order to obtain the cyclic loading on the track, a fixed observation point was set on the track, as each wheel on the train passes

Table 1. Computational parameters of ballast.

Parameters	Value	Parameters	Value
Density/kg/m^3	2,545	Young's modulus/Pa	5×10^9
Friction factor	0.3–0.9	Poisson ratio	0.22
Normal stiffness/N/m	3×10^7	Shear stiffness/N/m	2.6×10^6
Average diameter/m	0.035	Width/m	0.23
Height/m	0.3	Length/m	2.0
Particle amount	10,098	Clump amount	1,727

Table 2. Material parameters of the embankment and foundation.

	γ kN/m^3	E MPa	v	C kN/m^2	φ°
Embankment	20	25	0.3	10	15
Foundation	27	300	0.3	—	—

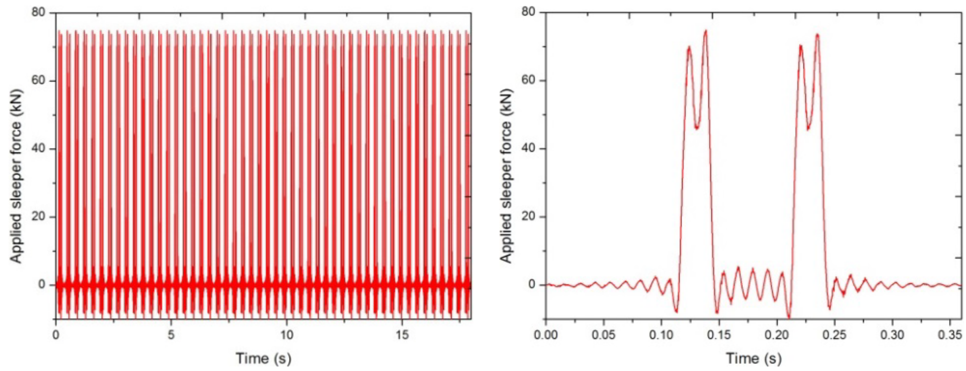

(a) (b)

Fig. 12. Time history of the applied cyclic loading on sleeper.

through the observation point, a peak value is detected [Paolucci *et al.* (2003)]. In this paper, sleeper is treated as a grid body due to its deformation which is not obvious in the whole railway structure. The cyclic loading is applied to the upper surface of sleeper uniformly.

Figure 13(a) shows the accumulated settlement of the sleeper. The simulation result shows that the settlement of sleeper changes acutely in the first three cycles, then drops steadily in the following cycles. It is mainly because of the loose packing of ballast particles initially. Under the cyclic loading, ballast particles move and rotate, and the rearrangement of ballast particles causes the rapid increase in the settlement of sleeper. However, the settlement drops slightly due to the denser arrangement of ballast particles as the number of cycle increases.

Figures 13(b) and 13(c) show the accumulated settlement of the top surface of the embankment and the top surface of the foundation, respectively. Twelve observation points are set to collect the settlements of different parts in the track structure, as show in Fig. 7. Six are located on the top surface of the embankment and the other six are located on the top surface of the foundation with the same x- and y-coordinates as those on the top of the embankment. Simulation results show a much smaller settlement of embankment and foundation, and a much smoother decline compared with that of the sleeper. The reasons are: (1) Due to the large initial voids, positions of ballast particles are not stable enough at the beginning. As a consequence, the applied load is first used to move and rotate ballast particles to get a stable packing, then further transferred to the embankment and foundation. (2) Due to the material properties, the cyclic loading is not large enough to generate an obvious unrecoverable plastic deformation in the embankment and foundation. Only the second observation point in Fig. 13(b) performs plastic behavior. The results also indicate the settlements of those point located under the sleeper are much larger than others.

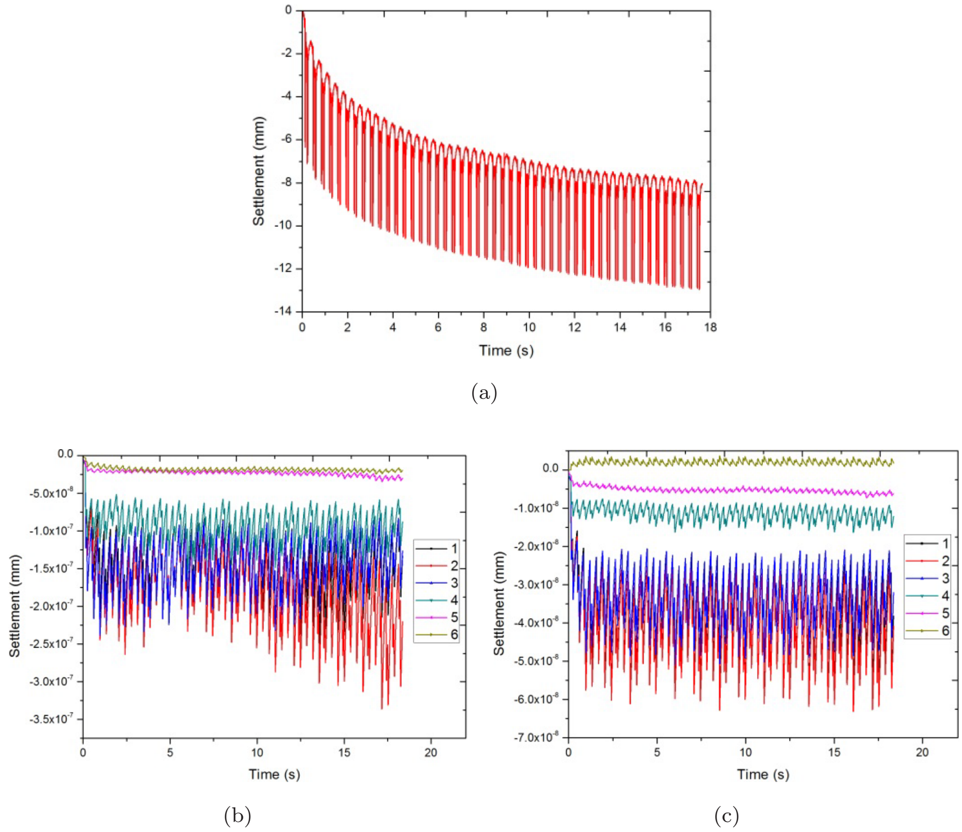

Fig. 13. Simulated settlement of (a) sleeper, (b) embankment and (c) foundation.

Figure 14 shows the force chains developed inside the ballast layer and stress distribution in the embankment and foundation at different stages of cyclic loading at the minimum loading and at the maximum loading. The brown area represents ballast particles and the blue lines represent force chains. Small contact forces are neglected in order to show the development of force chains more clearly. The force chains mainly develop beneath the sleeper. Moreover, the maximum value of the stress in the embankment and foundation layer is 20 kPa, which is much smaller than that in the ballast layer 210 kPa. This indicates that ballast can transmit the large traffic load to its underlying layers at an acceptable stress level. The stress distribution in substructures agrees with the force chains development in ballast.

Figure 15 shows the displacement of the embankment and foundation at the maximum loading. The displacement of the embankment is more obvious than that of the foundation. According to the distribution of force chains in ballast, the main

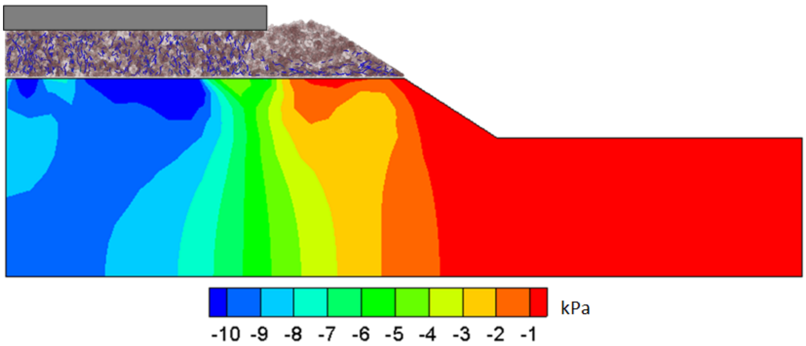

(a)

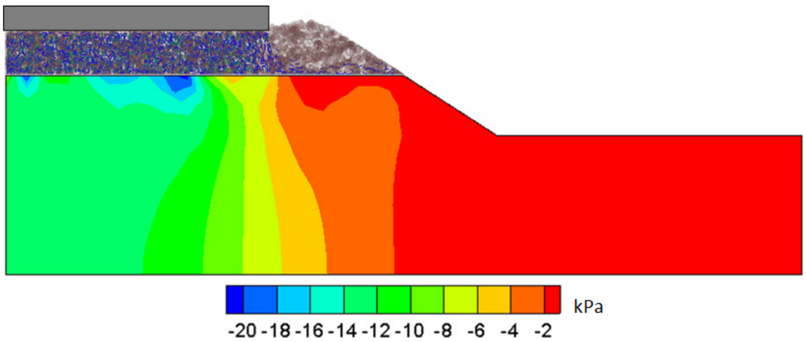

(b)

Fig. 14. (Color online) Force chains development and stress distribution at different loading stages: (a) at the minimum loading; (b) at the maximum loading.

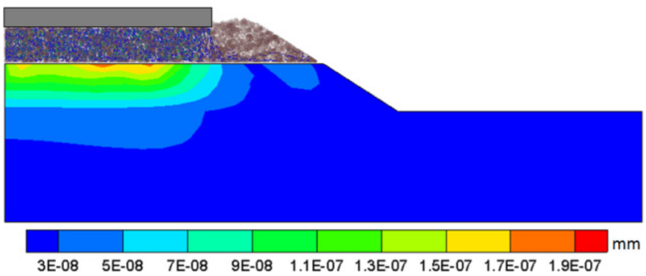

Fig. 15. Displacement of the embankment and foundation at maximum loading.

deformed region is also located in the area beneath sleeper. Figure 16 shows the accumulated plastic straincontour of the embankment and foundation. The plastic zone is located in the interior area of embankment and does not cut through the whole structure. The railway structure is stable under the applied traffic load.

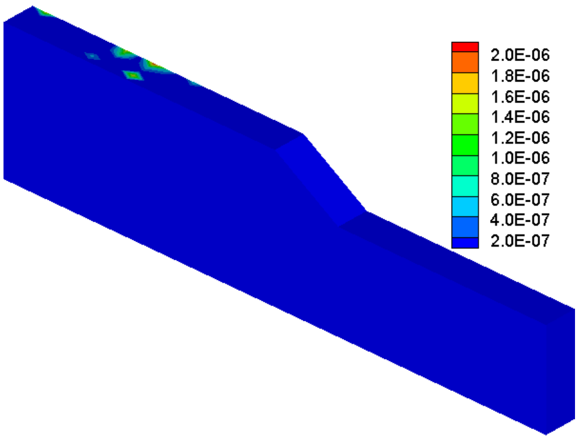

Fig. 16. Accumulated plastic strain contour of the embankment and foundation layers.

4. Conclusions

A combined discrete–finite element model is developed to analyze the dynamic behavior of ballasted railway track and the interaction between them. Simulation results show that the accumulated vertical settlement of sleeper mainly comes from the rearrangement of ballast particles and the settlement of substructure such as embankment and foundation. Through the force chains analysis of ballast, the ballast material can disperse the traffic loads to substructure, which can enhance the bearing capacity of substructure. The distribution of stress in substructure agreed with the development of force chains in ballast. The applied loads, for the most part, were sustained by the area under sleeper. Due to the higher strength of foundation, the deformation of embankment is more obvious than that of foundation. Moreover, the plastic zone does not cut-through the substructure, which confirms the stability of substructure under the applied cyclic traffic loads.

The long term settlement of ballast track caused by particle breakage and permanent plastic deformation is a critical issue in the study of dynamic behavior of ballast track. However, the model proposed in this paper could not handle this issue so far. Mainly, the restrictions are the low computational efficiency of DEM and the rigid body property of clump. In the future work, the GPU parallel computing will be employed to accelerate the calculation program. Moreover, the bond model will be introduced to simulate the ballast breakage.

Acknowledgments

This study is financially supported by the National Natural Science Foundation of China (41176012, U12342092, 11572067) and the Fundamental Research Funds for the Central Universities of China (DUT15ZD105).

References

Chen, C., McDowell, G. and Thom, N. [2012] "Discrete element modelling of cyclic loads of geogrid-reinforced ballast under confined and unconfined conditions," *Geotext. Geomembranes* **35**, 76–86.

Coleri, E., Harvey, J. T., Yang, K. and Boone, J. M. [2012] "Development of a micromechanical finite element model from computed tomography images for shear modulus simulation of asphalt mixtures," *Constr. Build. Mater.* **30**, 783–793.

Cundall, P. A. [1988] "Formulation of a three-dimensional distinct element model-Part I. A scheme to detect and represent contacts in a system composed of many polyhedral blocks," *Int. J. Rock Mech. Min. Sci. Geomech. Abstr.* **25**, 107–116.

Cundall, P. A. and Strack, O. D. L. [1979] "A discrete numerical model for granular assemblies," *Géotechnique* **12**, 47–65.

Di Renzo, A. and Di Maio, F. P. [2005] "An improved integral non-linear model for the contact of particles in distinct element simulations," *Chem. Eng. Sci.* **60**, 1303–1312.

Ei Kacimi, A., Woodward, P., Laghrouche, O. and Medero, G. [2013] "Time domain 3D finite element modelling of train-induced vibration at high speed," *Comput. Struct.* **118**, 66–73.

Ferellec, J. and McDowell, G. [2010] "Modelling realistic shape and particle inertia in DEM," *Géotechnique* **60**, 227–232.

Ghauch, Z. G., Ozer, H. and Ai-Qadi, I. L. [2015] "Micromechanical finite element modeling of moisture damage in bituminous composite materials," *Constr. Build. Mater.* **80**, 9–17.

Guo, L., Xiang, J., Latham, J. P. and Izzuddin, B. [2016] "A numerical investigation of mesh sensitivity for a new three-dimensional fracture model within the combined finite-discrete element method," *Eng. Fract. Mech.* **151**, 70–91.

Hai, Q. [2013] "Automatic generation of 2D micromechanical finite element model of silicon–carbide/aluminum metal matrix composites: Effects of the boundary conditions," *Mater. Des.* **44**, 446–453.

Huang, H. and Tutumluer, E. [2011] "Discrete element modeling for fouled railroad ballast," *Constr. Build. Mater.* **25**, 3306–3312.

Indraratna, B., Ngo, N. T., Rujikiatkamjorn, C. and Sloan, S. W. [2015] "Coupled discrete element-finite difference method for analyzing the load-deformation behavior of a single stone column in soft soil," *Comput. Geotech.* **63**, 267–278.

Indraratna, B., Ngo, N. T., Rujikiatkamjorn, C. and Vinod, J. [2012] "Behavior of fresh and fouled railway ballast subjected to direct shear testing: Discrete element simulation," *Int. J. Geomech.* **14**, 34–44.

Kremmer, M. and Favier, J. [2001] "A method for representing boundaries in discrete element modelling — part II: Kinematics," *Int. J. Numer. Methods Eng.* **51**, 1423–1436.

Laryea, S., Baghsorkhi, M. S., Ferellec, J. F., Well, G. R. and Chen, C. [2014] "Comparison of performance of concrete and steel sleepers using experimental and discrete element methods," *Transp. Geotech.* **1**, 225–240.

Leshchinsky, B. and Ling, H. I. [2013] "Numerical modeling of behavior of railway ballasted structure with geocell confinement," *Geotext. Geomembranes* **36**, 33–43.

Li, W., Dwight, R. A. and Zhang, T. [2015] "On the study of vibration of a supported railway rail using the semi-analytical finite element method," *J. Sound Vib.* **345**, 121–145.

Lim, W. and McDowell, G. [2005] "Discrete element modelling of railway ballast," *Granul. Matter* **7**, 19–29.

Lobo-Guerrero, S. and Vallejo, L. E. [2006] "Discrete element method analysis of rail track ballast degradation during cyclic loading," *Granul. Matter* **8**, 195–204.

Lu, M. and McDowell, G. [2007] "The importance of modelling ballast particle shape in the discrete element method," *Granul. Matter* **9**, 69–80.

Lu, M. and McDowell, G. [2010] "Discrete element modelling of railway ballast under monotonic and cyclic triaxial loading," *Géotechnique* **60**, 459–467.

Nejad, R. M. [2014] "Using three-dimensional finite element analysis for simulation of residual stresses in railway wheels," *Eng. Fail. Anal.* **45**, 449–455.

Ngo, N. T., Indraratna, B. and Rujikiatkamjorn, C. [2014] "DEM simulation of the behaviour of geogrid stabilised ballast fouled with coal," *Comput. Geotech.* **55**, 224–231.

Onate, E. and Rojek, J. [2004] "Combination of discrete element and finite element methods for dynamic analysis of geomechanics problems," *Comput. Methods Appl. Mech. Eng.* **193**, 3087–3128.

Paolucci, R., Maffeis, A., Scandella, L., Stupazzini, M. and Vanini, M. [2003] "Numerical prediction of low-frequency ground vibrations induced by high-speed trains at Ledsgaard, Sweden," *Soil Dyn. Earthq. Eng.* **23**, 425–433.

Peters, B. and Džiugys, A. [2002] "Numerical simulation of the motion of granular material using object-oriented techniques," *Comput. Methods Appl. Mech. Eng.* **191**, 1983–2007.

Potyondy, D. and Cundall, P. A. [2004] "A bonded-particle model for rock," *Int. J. Rock Mech. Min. Sci.* **41**, 1329–1364.

Ramirez, R., Poschel, T. and Brilliantov, N. V. [1999] "Coefficient of restitution of colliding visco-elastic sphere," *Phys. Rev. E* **60**, 4465–4472.

Real, J. I., Gómez, L., Montalbán, L. and Real, T. [2012] "Study of the influence of geometrical and mechanical parameters on ballasted railway tracks design," *J. Mech. Sci. Technol.* **26**, 2837–2844.

Rojek, J. and Onate, E. [2007] "Multiscale analysis using a coupled discrete/finite element model," *Interact. Multiscale Mech.* **1**, 1–31.

Rousseau, J., Frangin, E., Marin, P. and Daudeville, L. [2009] "Multidomain finite and discrete elements method for impact analysis of a concrete structure," *Eng. Struct.* **31**, 2735–2743.

Selig, E. T. and Waters, J. M. [1994] *Track Geotechnology and Substructure Management* (Thomas Telford, New York).

Shahraki, M., Warnakulasooriya, C. and Witt, K. J. [2015] "Numerical study of transition zone between ballasted and ballastless railway track," *Transp. Geotech.* **3**, 58–67.

Wang, Z., Jing, G., Yu, Q. and Yin, H. [2015] "Analysis of ballast direct shear tests by discrete element method under different normal stress," *Measurement* **63**, 17–24.

Winkel, B. [2010] "Viscous nonlinearity in central difference and newmark integration schemes," *Acta Mech.* **209**, 179–186.

Yan, Y. and Ji, S. [2010] "Discrete element modeling of direct shear tests for a granular material," *Int. J. Numer. Anal. Methods Geomech.* **34**, 978–990.

Yan, Y., Zhao, J. and Ji, S. [2014] "Discrete element analysis of breakage of irregularly shaped railway ballast," *Geomech. Geoeng.* 1–9.

AQ: Please provide Vol. no.

Vol. is **10**

Zhai, W., He, Z. and Song, X. [2010] "Prediction of high-speed train induced ground vibration based on train-track-ground system model," *Earthq. Eng. Eng. Vib.* **9**, 545–554.

Zhao, D., Nezami, E. G., Hashash, Y. M. and Ghaboussi, J. [2006] "Three-dimensional discrete element simulation for granular materials," *Eng. Comput.* **23**, 749–770.